

# Retrieval of Surface Wave Parameters from SAR Images and Their Validation in the Coastal Seas around Japan

JIAN SUN<sup>1\*</sup> and HIROSHI KAWAMURA<sup>2</sup>

<sup>1</sup>Physical Oceanography Laboratory, Ocean University of China, Qingdao 266100, China

<sup>2</sup>Ocean Environment Group, Center for Atmospheric and Oceanic Studies, Graduate School of Science, Tohoku University, Sendai 980-8578, Japan

(Received 3 August 2007; in revised form 3 May 2009; accepted 4 May 2009)

We have developed a scheme to retrieve surface wave parameters (wave height and wave propagation direction) from European Remote-Sensing Satellite (ERS) Synthetic Aperture Radar (SAR) image mode data in coastal seas around Japanese coastlines. SAR spectra are converted to surface wave spectra of swell-dominated or wind-wave dominated cases. The SAR spectrum and SAR-derived wind speed are used to derive the surface wave spectrum. The wind-wave dominated case and swell-dominated case are differentiated by a wind speed of 6 m/s, and processed in different ways because of their different degree of nonlinearity. It is indicated that the cutoff wavelength for retrieval of the wind-wave dominated spectrum is proportional to the root of significant wave height, which is consistent with the results of previous studies. We generated 66 match-ups using the SAR sub-images and the in-situ surface wave parameters, which were measured by wave gauges installed in near-shore seas. Among them, there are 57 swell-dominated cases, and 9 wind-wave dominated cases. The significant wave heights derived from SAR and from in-situ observation agree with the bias of 0.09 m, the standard deviation of 0.61 m and the correlation coefficient of 0.78. The averaged absolute deviation of wave propagation directions is 18.4°, and the trend of the agreement does not depend on the wave height. These results demonstrate that the SAR surface wave spectrum retrieved by the present system can be used to observe the surface wave field in the coastal seas around Japan.

Keywords:

- Synthetic Aperture Radar,
- surface wave spectrum,
- SAR spectrum,
- SAR wind speed,
- coastal sea,
- surface wave retrieval.

## 1. Introduction

One of the functions of Synthetic Aperture Radar (SAR) in oceanography is to observe the surface wave field. An accumulated, large volume of SAR images contains a variety of surface wave information, and this is still an important research target. Retrieval of the surface wave spectrum from SAR images has been studied by many researchers (Hasselmann and Hasselmann, 1991; Engen and Johnsen, 1995; Hasselmann *et al.*, 1996; Mastenbroek and de Valk, 2000; Schulz-Stellenfleth *et al.*, 2005).

It is generally accepted that the mechanism underlying SAR imaging of surface waves is that Bragg waves, which backscatter the SAR microwaves, are modulated through the interaction with longer surface waves (Alpers, 1983). Different modulation mechanisms act at different

phases of the longer waves, which creates the wave-like stripe patterns in SAR images. The major modulation mechanisms are tilt modulation, hydrodynamic modulation and velocity bunching, which are modeled by the modulation transfer functions for the SAR wave imaging (Wright, 1978; Alpers *et al.*, 1981; Monaldo and Beal, 1998). On the basis of the modulation theories (Hasselmann *et al.*, 1985), a closed spectral integral transform relationship between the SAR spectra and the surface wave spectra has been proposed and has become widely accepted (Hasselmann and Hasselmann, 1991).

In the retrieval of SAR wave spectra, the method called Max-Planck Institute Algorithm (MPI) needs a first-guess spectrum, which is derived from the outputs of the numerical wave model WAM (Hasselmann and Hasselmann, 1991; Hasselmann *et al.*, 1996). Mastenbroek and de Valk (2000) have developed a spectral inversion algorithm (Semi Parametric Retrieval Algorithm Scheme, SPRA), which needs the SAR image spectra and the satellite scatterometer wind vector meas-

\* Corresponding author. E-mail: sunjian77@ouc.edu.cn

urement. Through comparisons between the SAR-derived wave parameters and buoy observations for 6 years, Voorrips *et al.* (2001) have concluded that the SPRA results are more accurate than those of MPI.

Coastal seas are important for a variety of human activities, such as transportation, fisheries, tourism etc. Surface wave dynamics become more complex in the coastal seas than that in the deep ocean. It is well known that the wave model result is distorted by the dominance of swell and the dramatic change of water depth (Elgar *et al.*, 1994). Therefore, the SAR observation becomes an important way to acquire the surface wave information. Using the ERS SAR wave mode data, applications of the SAR-wave information are well developed in the open oceans. Although a large volume of the SAR images illuminating coastal seas are archived in the satellite data centers, the coastal application of SAR wave information is pre-mature, due to limited knowledge about SAR retrieval of the coastal wave parameters and a lack of comprehensive validation. Collard *et al.* (2005) examined the surface wave spectra derived from ENVISAT-ASAR in the coastal seas near France. Their case study has shown great potential of high-resolution SAR image for coastal surface wave monitoring.

In this study we have developed a system to retrieve the surface wave parameters from high-resolution SAR images around the coastal seas of Japan. This is the first systematic validation of the SAR-retrieved wave parameters for the seas close to the Japanese coast. In the absence of any additional information as input for the retrieval, we use SAR-derived surface wind together with the SAR spectra. The swell-dominated cases and wind-wave dominated cases, which are differentiated by the SAR wind speed, are processed in different schemes. The SAR wave parameters are validated by wave gauge measurements around Japanese coastlines. The observation data and match-up generation are introduced in Section 2. The retrieval method is presented in Section 3, and the results of retrieval are given in Section 4 with their validation. Conclusions and discussions are presented in Section 5.

## 2. Data and Match-Up Generation Method

ERS-1 and ERS-2 were launched in 1991 and 1995, respectively. They carried an Active Microwave Instrument (AMI), which has a SAR function operating in the C band with VV polarization. Its incident angle is limited to 20°–26°, making the swath of SAR images around 100 km. The SAR images are produced from the raw data received at the JAXA station using the Sigma-0 SAR Processor (Shimada, 1999). The SAR image mode data is formed by 6656 pixels in the azimuth direction and 5344 pixels in range. We use 5120\*5120 pixels of the original size, avoiding the interference of dark pixels around the

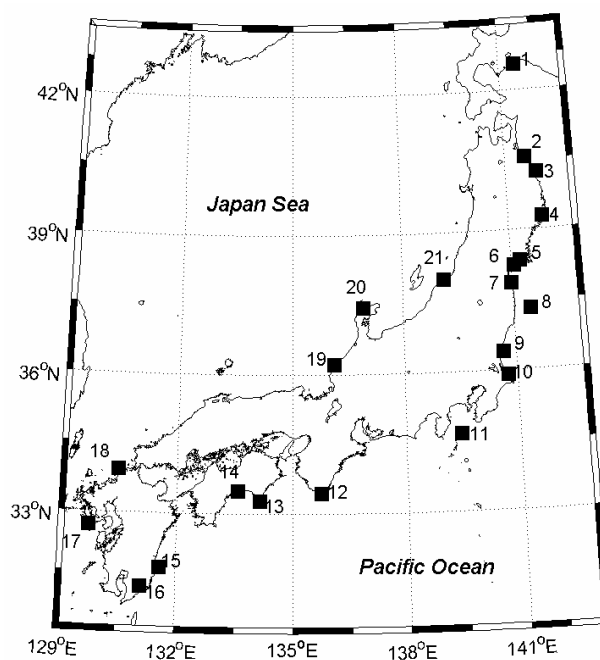


Fig. 1. Locations of the NOWPHAS wave gauges in the coastal seas around Japan.

image edges.

The NOWPHAS (Nationwide Ocean Wave information network for Ports and HARbourS) data we use in this study include wave-gauge measurements made at 21 stations, which are located at sites on the Japanese coastlines shown in Fig. 1 and described in Table 1. The wave sensors of NOWPHAS are an Ultra-sonic Wave Gauge (UWG), a Current meter type Wave Directional meter (CWD) and a newly developed wave-directional meter (DWDM). These sensors are mounted on the sea bottom at depths ranging from 17 to 55 meters, except for the surface sensor at No. 8 station (Table 1). The NOWPHAS wave information we used is mean wave propagation directions, significant wave heights and significant wave periods, which are sampled every two hours. The NOWPHAS wave gauge data are used for real-time coastal wave observation after necessary data correction and reconciliation (Nagai and Nukada, 2004). In our analyses, abnormal values of the past NOWPHAS data are searched using data flags added by the NOWPHAS quality control, and excluded in the match-up generation process described below. Because there are no spectral information and no other wave parameters from the in situ data source, our validation of the SAR-derived parameters is limited to the wave direction and the significant wave height.

Match-ups are generated by combining coincident

Table 1. NOWPHAS wave gauges used in this study.

No.	Name	Position	Instrument depth (m)	Instrument	Wave direction observation from
1	TOMAKOMAI	42°39'06" 143°41'08"	23	DWDM	2002.12
2	HACHINOHE	40°33'39" 141°34'06"	27.7	CWD	1991.01
3	KUJI	40°13'04" 141°51'36"	49.5	DWDM	1996.04
4	KAMAISHI	39°15'54" 141°56'06"	49.8	USW	\
5	ISHINOMAKI	38°20'48" 141°15'18"	20	CWDDWDM	1995.04
6	SHENDAI-KOKU	38°15'00" 141°03'58"	21.3	USWCWD	1991.01
7	SOMA	37°51'28" 140°58'52"	17.1	USWCWD	1991.01
8	IWAKI-OKI	37°18'00" 141°27'35"	surface	SRW-VCWD	1986.10
9	JYOBANNAKA	36°23'42" 140°39'12"	30.3	USWCWD	1991.01
10	KASHIMA	35°53'55" 140°45'14"	24	CWD	1991.07
11	NAMIUKI	34°40'31" 139°26'19"	29.7	CWD	1991.01
12	SHIONOMISAKI	33°25'59" 135°44'50"	54.7	DWDM	1999.02
13	MUROTSU	33°16'16" 134°08'52"	26.8	USWCWD	1991.01
14	KOCHI	33°28'57" 133°35'13"	24.1	DWDM	1997.08
15	MIYAZAKI	31°49'20" 131°34'58"	32	USWCWD	1991.01
16	SHIBUSHIWAN	31°25'02" 131°06'36"	36.2	CWD	1991.11
17	IOUJIMA	32°42'59" 129°45'15"	31.9	CWD	1992.11
18	GENKAINADA	33°56'02" 130°28'05"	39.5	CWDDWDM	1991.01
19	KANAZAWA	36°36'50" 136°34'02"	20.2	USW	\
20	WAJIMA	37°25'51" 136°54'08"	52	CWDDWDM	1991.01
21	NIGATAOKI	38°00'17" 139°07'34"	34.5	CWDDWDM	1989.11

SAR sub-images and NOWPHAS wave gauge data. The SAR image of 5120\*5120 pixels is divided into 40\*40 sub-images, which have 128\*128 pixels (approximately 1.6\*1.6 km). The match-up is a couple comprising the SAR sub-image whose center is the closest to the wave-gauge location (Table 1 and Fig. 1), and the in situ wave information. Their maximum time difference is one hour thanks to the NOWPHAS sampling rate of two hours. If one of the three kinds of in situ wave information is not available within one hour of the SAR imaging time, we did not make the match-up. We use several criteria for match-up generation. If the distance between the sub-image center and the wave gauge location is longer than 0.5° (corresponding to 45.6 km in the latitude direction and to 55.5 km in the longitude direction), the match-up is not generated. We calculate the SAR wave spectrum of coupled sub-images. If the ratio of the spectral peak to background levels is less than 3, the match-up is void. Using the ERS SAR images during 1991 to 2003, we obtained 98 match-ups. With the same sensor specifications and the same data processor, the images of ERS-1 and ERS-2 SAR show no quality difference and thus no characteristic difference between the SAR spectra from ERS-1 SAR and that from ERS-2.

The generated match-ups were carefully checked one by one, and 32 match-ups were found to be void (see Ta-

ble 2). When we judge that propagating waves in a sub-image are blocked by undulating coastlines or islands and not well observed by the wave gauge, we rejected the match-up (16 match-ups, topography in Table 2). If surface wave stripes in the sub-image are deteriorated by other phenomena, e.g., atmospheric front, internal waves, unclassified black areas etc., the match-ups are voided (16 match-ups, image quality in Table 2). Finally, 66 of the 98 match-ups generated (about 70%) passed the manual check mentioned above.

### 3. Retrieval of Coastal Surface Wind and Wave Spectra from SAR Images

#### 3.1 SAR coastal surface winds

The ERS-SAR normalized radar cross section (NRCS) calibration for the produced SAR image mode data is given by Shimada (1999). The calibrated NRCS of every pixel in dB is given by the following equation (1)

$$NRCS = 20 \log_{10}(DN) + CF, \quad (1)$$

where CF is the ERS calibration parameter and DN is the output of the Sigma-0 processor.

The wind retrieval for C-Band and L-Band SARs has

Table 2. Match-up data classification.

Sample accepted	Swell	57
	Wind wave	9
Sample rejected	Topography	16
	Image quality	16
Total		98

been studied by many researchers (Alpers *et al.*, 1998; Pan and Smith, 1999; Furevik *et al.*, 2002; Shimada *et al.*, 2003). Shimada and Kawamura (2005) have derived the high-resolution surface wind information from about 6,500 ERS SAR scenes in the coastal seas around Japan. They used the empirical coefficient of the model function named CMOD\_IFR2 and the wind direction of reanalysis data produced by National Center for Environmental Prediction/National Center for Atmospheric Research (NCEP/NCAR) for the retrieval. The root mean square errors of SAR-derived wind speeds are about or less than 2 m/s against in-situ and scatterometer measurements (Shimada *et al.*, 2004; Shimada and Kawamura, 2005; Yamaguchi and Kawamura, 2005). Therefore, the SAR-derived wind speeds have suitable quality for the present study. The SAR wind speeds with the resolution of around  $1 \text{ km}^2$  within a specific sub-image used for deriving the SAR spectrum (approximately  $2.5 \text{ km}^2$ ) is averaged to make the match-ups for the present study. Note that we use the simultaneously obtained SAR wind together with the SAR spectra for retrieval the surface wave spectra whereas SPRA (Mastenbroek and de Valk, 2000) used the scatterometer wind vectors.

### 3.2 Coastal surface wave spectra

Figure 2 shows a flow chart for the retrieval procedure of the SAR surface wave parameters (significant wave height and wave propagation direction), which we describe below.

The SAR sub-image is first filtered using a Gaussian high-pass filter to remove the low wave number signal which has no relation to surface waves. Figure 3(a) shows the high-pass filtered sub-image and Fig. 3(b) the coarse SAR spectra computed from it by 2-dimensional Fast Fourier Transform (2-D FFT). The smoothed SAR spectrum is derived by applying a low-pass filter to the coarse spectra with the conservation of spectral energy.

Generally, it is considered that the SAR spectrum  $P_{obs}(\mathbf{k})$  is a combination of a wave image spectrum  $P_f(\mathbf{k})$  and a background clutter noise spectrum  $P_{cl}(\mathbf{k})$  (Bruning *et al.*, 1994; Hasselmann *et al.*, 1996). To the first order,  $P_{obs}(\mathbf{k}) = P_f(\mathbf{k}) + P_{cl}(\mathbf{k})$ , which means that the modulation of clutter noise by the ocean waves is negligible. The

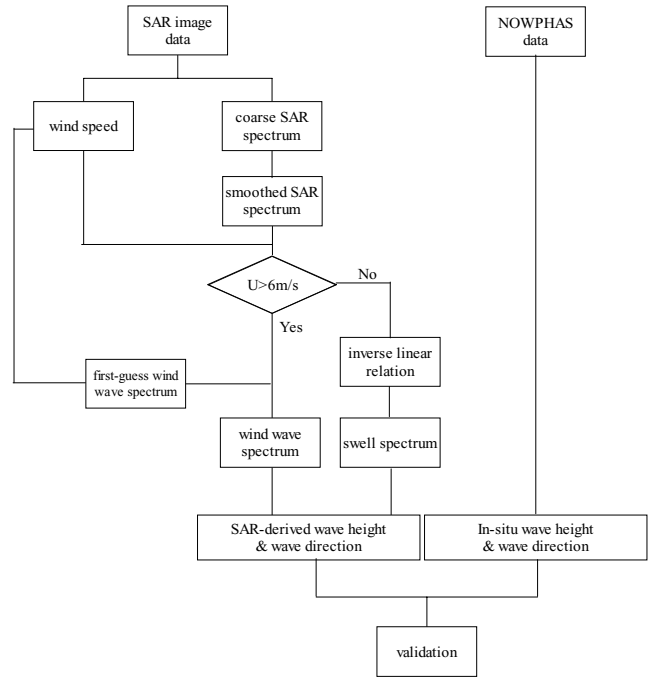


Fig. 2. Flow chart of retrieval of the SAR surface wave parameters.

clutter spectrum can thus be removed by subtraction. Below the high wave number roll-off due to the system impulse response function, the clutter spectrum is essentially white (Alpers and Hasselmann, 1982). We estimate the clutter noise spectrum by averaging SAR-spectrum density of the first 10 bins near the Nyquist wave number. The derived  $P_f(\mathbf{k})$  image is illustrated in Fig. 3(c).

We treat swell-dominated SAR spectrum  $P_{I-S}(\mathbf{k})$  and wind-sea dominated SAR image spectrum  $P_{I-W}(\mathbf{k})$  in a different way (Fig. 2). The differentiating criteria are discussed in detail in Section 4. For the swell-dominated case, we retrieve the surface wave spectrum by linear image relationship  $P_{I-S}(\mathbf{k}) = k^2[|T(\mathbf{k})|^2F(\mathbf{k}) + T(-\mathbf{k})|^2F(-\mathbf{k})]$  giving the standard modulation transfer function (Lyzenga, 1986; Feindt *et al.*, 1986; Hasselmann and Hasselmann, 1991). In principal, the SAR spectrum has  $180^\circ$  directional ambiguity. In order to remove the directional ambiguity, we adopt the fact that swell can only propagate toward the coast. Since all the SAR images used in the present study are matched with the wave gauge stations at Japanese coastlines, their identification is easy.

For the wind-sea dominated case in Fig. 3, we use the JONSWAP spectrum (Hasselmann *et al.*, 1973; Hasselmann *et al.*, 1980) and the wave directional spreading function proposed by Donelan *et al.* (1985) to construct a parameterized wind wave spectrum as a first-guess spectrum  $\hat{F}(\mathbf{k})$ .  $\hat{F}(\mathbf{k})$  is the wave number spectrum which

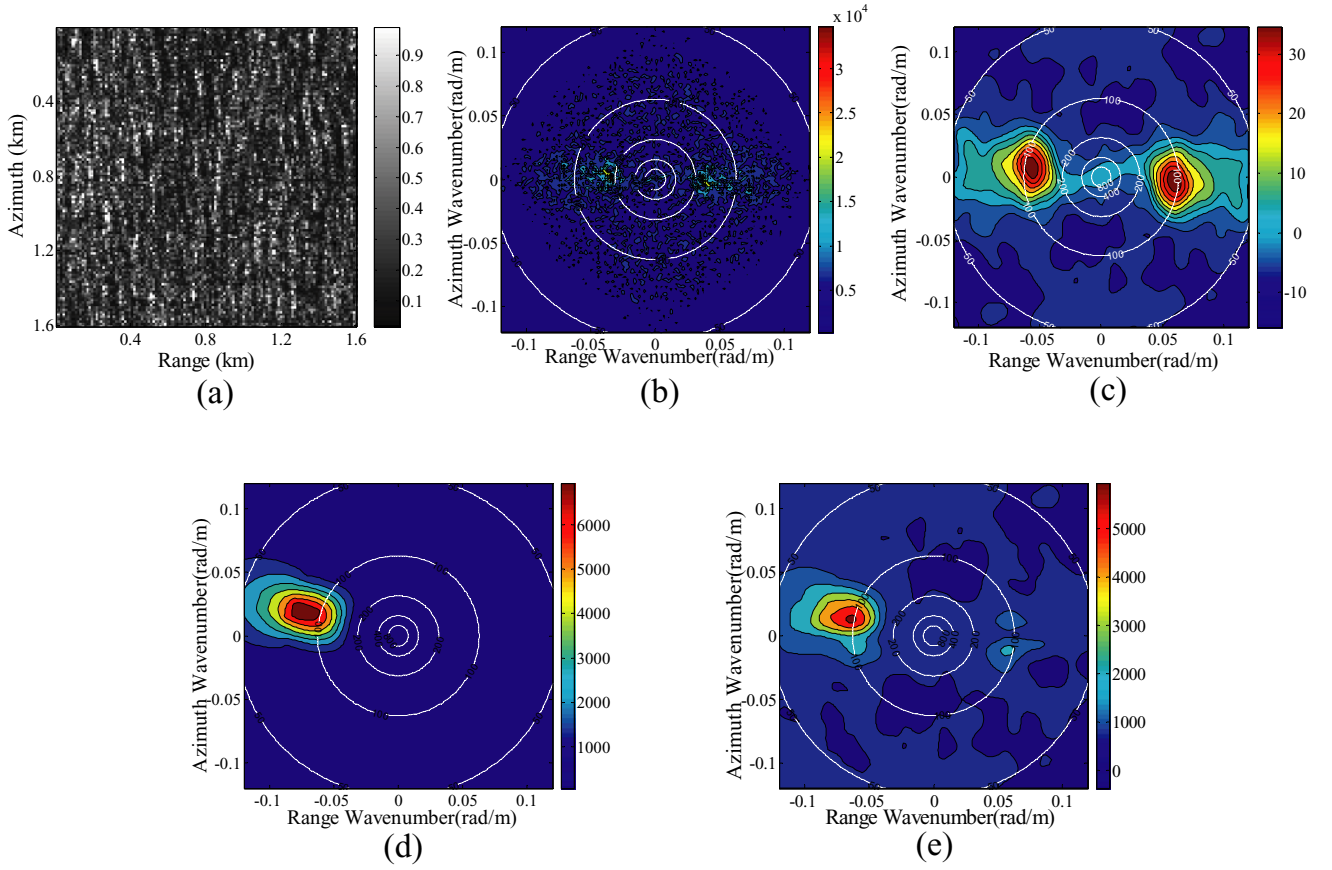


Fig. 3. Example of processing for retrieving wind-wave spectrum from a SAR image. (a) SAR sub-image of 128\*128 pixels, (b) original SAR image spectrum, (c) filtered SAR image spectrum, (d) first guess spectrum constructed by the JONSWAP model using SAR wind speed, and (e) retrieved wave spectrum.

is derived by transforming from the frequency direction spectrum

$$S(\omega, \theta) = \frac{1}{2} S(\omega) \beta \operatorname{sech}^2 \beta [\vartheta - \vartheta_m], \quad (2)$$

$$S(\omega) = \alpha \frac{g^2}{\omega^5} \exp \left[ -1.25 \left( \frac{\omega_0}{\omega} \right)^4 \right] \gamma \exp \left[ \frac{(\omega - \omega_0)^2}{2\sigma^2 \omega_0^2} \right], \quad (3)$$

where  $\alpha = 0.006(U_{10}/c_0)^{0.55}$ ,  $\sigma = 0.08(1 + 4(c_0/U_{10})^3)$  and the  $\omega_0$ ,  $c_0$  and  $U_{10}$  is peak frequency, peak phase speed and wind speed at 10 m height respectively.  $\gamma$  is peak enhancement factor and  $\beta$  is a function of frequency. The first-guess spectra are used to fill the gap beyond the azimuthal cut-off wavelength.

Using the nonlinear imaging mechanism  $P_{I-W}(\mathbf{k}) = \Phi(F(\mathbf{k}))$  (Hasselmann and Hasselmann, 1991; Krogstad *et al.*, 1994), we derive the best-fit surface wave spec-

trum  $F(\mathbf{k})$  and the best-fit SAR spectrum  $P(\mathbf{k})$  minimizing a cost function  $J$  through an iterative procedure. Hasselmann and Hasselmann (1991) used a cost function to estimate the wave directional spectra from the SAR spectra. The form of the cost function is expressed as follows.

$$J = \int [P(\mathbf{k}) - \hat{P}(\mathbf{k})]^2 d\mathbf{k} + \mu \int \left[ \frac{F(\mathbf{k}) - \hat{F}(\mathbf{k})}{B + \hat{F}(\mathbf{k})} \right]^2 d\mathbf{k}$$

$B$  is introduced to avoid the numerical infinity when  $\hat{F}(\mathbf{k}) = 0$ . Through careful examinations using the matchups which are applied for the following validation process, we find no zero value for  $\hat{F}(\mathbf{k})$  because of the selection of SAR sub-images with clear wave stripes. Moreover, the difference between  $F(\mathbf{k})$  and  $\hat{F}(\mathbf{k})$  is naturally scaled for the sub-images. On the basis of the above formulation, we simplified the form of cost function as follows.

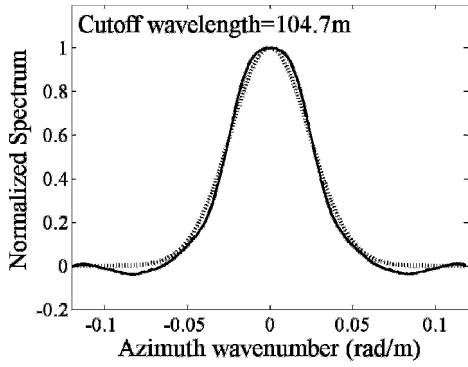


Fig. 4. An example of SAR spectrum in the azimuth direction and a fitted Gaussian function for calculating cutoff wavelength.

$$J = \int [P(\mathbf{k}) - \hat{P}(\mathbf{k})]^2 d\mathbf{k} + \mu \int [F(\mathbf{k}) - \hat{F}(\mathbf{k})]^2 d\mathbf{k}, \quad (4)$$

where  $\hat{P}(\mathbf{k})$  is the SAR spectrum derived from the SAR sub-image and  $\mu$  is a weighting coefficient (Hasselmann and Hasselmann, 1991). The weighting factor is set according to the reliability of the first-guess spectrum or observed SAR spectrum. In this study, the SAR wind and the empirical directional spectrum model are used to derive the first-guess spectrum which is less reliable than the observed SAR spectra, so the weighting factor is set to a small value, 0.1, by examination. An example of first-guess surface wave spectrum derived from the SAR wind speed (11 m/s) and direction ( $256^\circ$ ) is shown in Fig. 3(d). The best-fit surface wave spectrum indicated in Fig. 3(e) is derived through the iteration scheme described above (see Fig. 2 for this processing flow).

The SAR spectra are always affected by azimuth cutoff, the effect of SAR spectra roll-off in the azimuth direction. The azimuth cutoff is caused by the nonlinearity of the SAR surface-wave imaging mechanism in the azimuth direction and acts as a low-pass Gaussian filter to the SAR spectra. In the ERS SAR wave mode products (Johnsen *et al.*, 1999), the cutoff wavelength is a parameter derived by fitting a Gaussian function to the range-integral SAR spectrum (Vachon *et al.*, 1994; Kerbaol *et al.*, 1998; Schulz-Stellenfleth and Lehner, 2002). We follow the similar steps to estimate the cutoff wavelength for an appropriate coastal SAR spectrum.

It is well known that the azimuth cut-off is dominated in the SAR-spectra of wind-sea condition (Kerbaol *et al.*, 1998). Using the SAR surface wind, we choose the wind-wave cases in which the retrieved wind speeds are higher than 6 m/s. Because of the greater degree of imaging nonlinearity, the SAR spectra of wind-wave cases show that the wind waves travel in the range direction of the SAR image. Since the case shown in Fig. 3 has a cor-

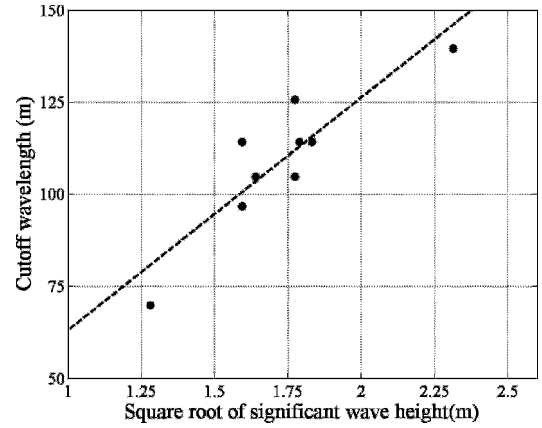


Fig. 5. Relationship between cutoff wavelength and square root of significant wave height. Least square best fit is indicated by the dashed line.

responding wind-speed of about 11 m/s, the spectrum in Fig. 3(c) has peaks located at low azimuth-angle because of the relatively great nonlinearity, i.e., the waves in the SAR image are propagating roughly in the range direction. The spectrum is integrated in the range direction of the SAR spectrum. The maximum value is located at the zero wave number and it is reasonable to fit it with a Gaussian function, which is formulated as,

$$\exp\left(-\pi\left(\frac{k_x}{k_c}\right)^2\right), \quad (5)$$

where  $k_c = 2\pi/L_c$  and  $L_c$  is the cutoff wavelength.  $k_x$  is the variable of Gaussian function. For the case of Fig. 3, the fitting result is illustrated in Fig. 4, together with the integrated spectrum.

Figure 5 shows the relationship between the cutoff wavelength and the square root of significant wave height, which is derived by the following equation.

$$H_s = 4.0 * \sqrt{m_0}, \quad (6)$$

where  $m_0 = \iint F(k_a, k_r) dk_a dk_r$ .  $k_a$  and  $k_r$  are the wave number in azimuth and range direction respectively. Although the number of match-up points for the wind-wave dominated condition are small ( $N = 9$ ), it is indicated that the cutoff wavelength is proportional to the square root of significant wave height  $\sqrt{H_s}$  with a correlation coefficient of 0.86. This relation is also presented by Vachon *et al.* (1994), although they examined relationships between the cutoff wavelength and other parameters (i.e., wind speed). In our study, we could not investigate its dependence on

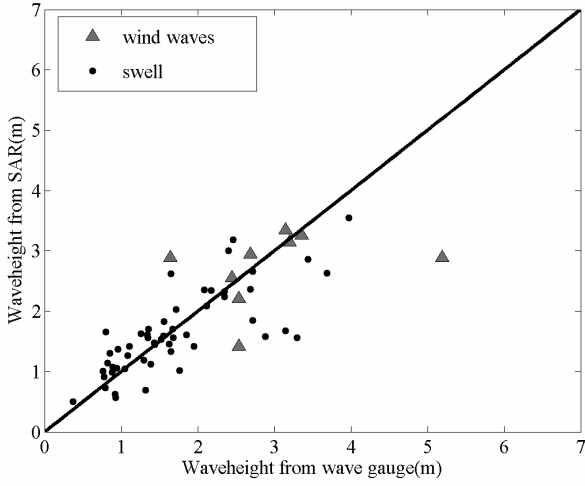


Fig. 6. Comparison between gauge-measured and SAR-derived significant wave heights. Solid line indicates perfect correlation. Solid circle dots indicate the significant wave heights of swell cases and the triangles indicates that of wind wave cases.

the other parameter because of the limited data set further examination of the cutoff wavelength is left for future studies.

On the other hand, owing to the weak imaging nonlinearity in the swell-dominated case, the propagation direction of swell is well detected in the SAR image. Therefore, when the wind-speed is less than 6 m/s in the match-up sub-image, we did not apply the wavelength estimate cut-off procedure.

### 3.3 Validation of the retrieved surface wave spectra

We now compare the surface-wave parameters obtained from the SAR image to the NOWPHAS surface-wave parameters. Figure 6 shows the comparison of SAR-derived significant wave height and the corresponding NOWPHAS significant wave height. The comparison shows an agreement with a bias of 0.07 m and standard deviation of error (SDE) of 0.61 m. The correlation coefficient between them is 0.78. The biases and the SDE for the wind-wave dominated cases (9 among 66 match-ups) are 0.19 m and 0.94 m and for the swell-dominated cases (57) 0.07 m and 0.53 m, respectively.

In our study, the SAR wave heights are underestimated against the NOWPHAS measurements. The reason may be attributed to cut-off of the wave spectrum in the higher wave number domain caused by the limited SAR resolution. That is,

$$H_s = 4.0 \times \sqrt{\int_{-\infty}^{+\infty} \int_{-\infty}^{+\infty} F(\mathbf{K}) dk_a dk_r}$$

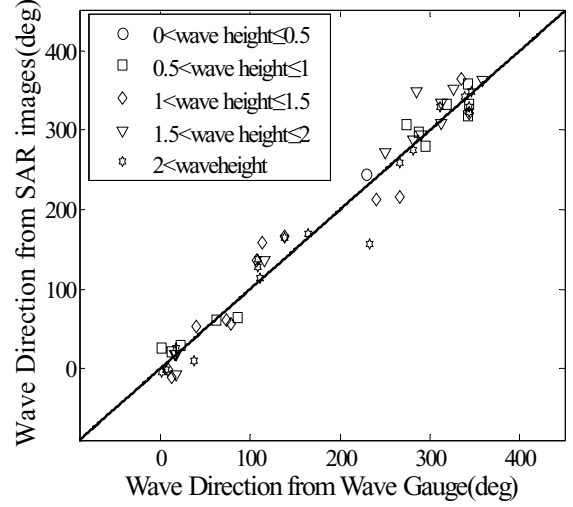


Fig. 7. Comparison between gauge-measured and SAR-derived wave propagation direction. Solid line indicates perfect correlation. Five groups of samples categorized by wave height are shown: wave height less than 0.5 m (circle), between 0.5 m and 1 m (square), between 1 m and 1.5 m (diamond), between 1.5 m and 2 m (triangle) and larger than 2 m (hexagon).

$$> 4.0 \times \sqrt{\int_{-k_{Nr}}^{k_{Nr}} \int_{-k_{Na}}^{+k_{Na}} F(\mathbf{K}) dk_a dk_r},$$

where  $k_{Na}$  and  $k_{Nr}$  are the Nyquist wave numbers defined by the SAR spatial resolution.

Figure 7 shows the relationship between the characteristic wave directions from the SAR images and NOWPHAS. For wave gauge observation, the wave direction is characterized by the propagation direction of the significant wave component. The peak of the SAR surface wave spectrum gives the wave direction of the dominant wave according to the formula  $\theta_{SAR} = \arctan(k_y/k_x)$  where  $(k_x, k_y)$  is the wave number corresponding to the peak of retrieved wave spectrum. Since surface waves can be assumed as a stationary process with a spatially quasi-homogeneous distribution (samples under the effect of refraction are excluded when generating the match-ups; Table 2), the characteristic wave direction from NOWPHAS and the peak wave direction derived from SAR should be quantitatively the same. They agree with each other with averaged absolute deviation of 18.4°, as calculated by the formula

$$\frac{1}{n} \sum_{i=1}^n |\theta_{SAR} - \theta_{in\_situ}|$$

The agreement does not depend on the wave height, as

Table 3. Comparison between the wind-wave dominated and the swell-dominated conditions in terms of the SAR spectrum retrieval, and validation results.

Wind wave		Swell	
Imaging mechanism	Mostly nonlinear	Mostly linear	
Wave stripes in SAR image	Align in nearly range direction	Keep the real propagation direction	
Imaging relationship	$P_{r-w}(\mathbf{k}) = \Phi(F(\mathbf{k}))$	$P_{r-s}(\mathbf{k}) = k^2 [ T(\mathbf{k}) ^2 F(\mathbf{k}) +  T(-\mathbf{k}) ^2 F(-\mathbf{k})]$	
Retrieving method	Iteratively searching the best-fit wave spectra	Directly invert the linear imaging relation	
First guess spectrum	JONSWAP spectrum combined with directional function	Not consulted	
180° ambiguity	Referring to wind direction	Referring to coastline	
Validation			
Number of match-ups	9	57	
Bias (m)	0.19	0.07	
SDE (m)	0.94	0.53	
Error in mean wave direction	16.4°	18.7°	

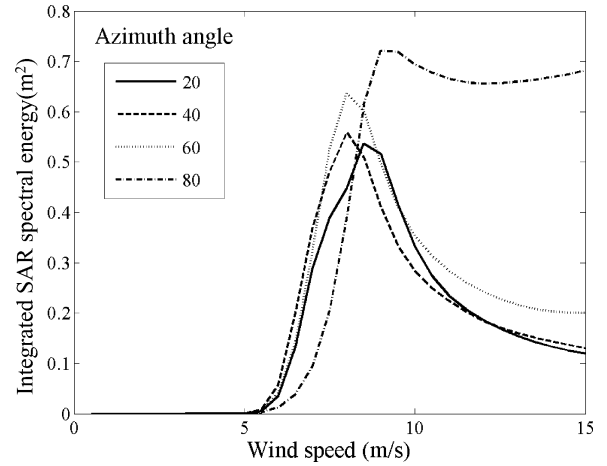


Fig. 8. Relationships between the integrated spectral energy within the Nyquist wave numbers and wind speed for different azimuth angles. SAR spectra are estimated using the present scheme.

indicated in Fig. 7. Our validation demonstrates that the developed SAR surface wave spectrum has sufficient accuracy for monitoring surface waves in the Japanese coastal seas.

#### 4. Discussion

We used a criterion of 6 m/s to separate the wind-wave and swell dominated conditions. The difference of spectrum retrieval between the conditions is summarized in Table 3. We now discuss how reasonable it is.

The surface waves can only be detected by SAR images if the wavelength of the imaged waves is greater than the SAR spatial resolution. To determine whether or not the surface waves recognized by the limited spatial resolution of SAR image are generated by wind, we simulate the relationship between the SAR spectra energy and the wind speed. The integrated spectrum energy within the Nyquist wave numbers ( $E_{Nyquist}$ ) can be formulated as:

$$E_{Nyquist} = \int_{-\pi/\rho_r}^{\pi/\rho_r} \int_{-\pi/\rho_a}^{\pi/\rho_a} P_{SAR}(\mathbf{k}) dk_a dk_r,$$

where  $P_{SAR}(\mathbf{k})$  is the SAR spectrum derived from the parameterized wave spectrum and HH-relationship, and  $\rho_r$  and  $\rho_a$  are the resolutions of SAR images in range and azimuth directions, respectively. As mentioned above, the selection criterion of 6 m/s is based on a consideration of the imaging capability of ERS-1/2 SARs. When the SAR resolution of  $\rho_r$  and  $\rho_a$  increases, the shorter components of surface wave can be observed by the SAR, which may reduce this wind speed criterion.

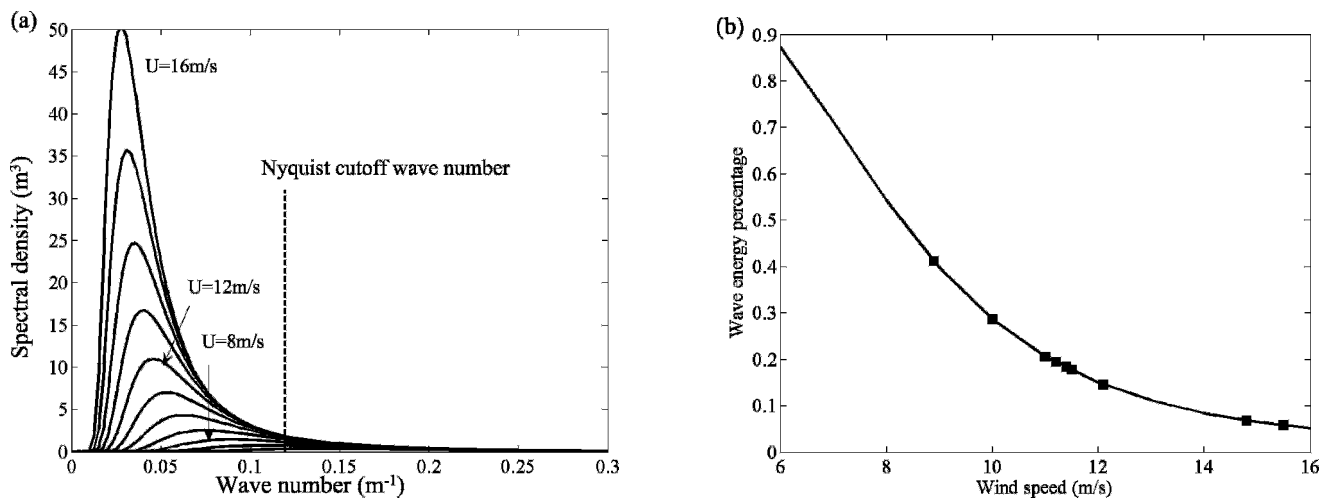


Fig. 9. (a) JONSWAP spectra at different wind speeds ranging from 6 m/s to 16 m/s. Dashed line shows the Nyquist cutoff wave number according to the resolution of ERS SAR. (b) Ratio of wave energy beyond the cutoff wave number to the total wave energy, calculated from (a), at different wind speed (solid line). Solid square indicates wind wave cases examined in the present study.

Figure 8 shows the relationship between  $E_{Nyquist}$  and the wind speed at azimuth angles of  $20^\circ$ ,  $40^\circ$ ,  $60^\circ$  and  $80^\circ$ . The azimuth angle is defined as the angle between the wave (wind) and azimuth directions. As seen in Fig. 8,  $E_{Nyquist}$  is weak for wind speeds  $< 6$  m/s for any azimuth angles. When wind speed is less than 6 m/s, the wavenumbers of wind-wave peak are larger than the Nyquist wavenumbers. Because of the limited SAR spatial resolution, the dominant wind waves are detectable at wind speeds  $> 6$  m/s. If the wind speed  $< 6$  m/s, the SAR imaged surface waves are swell. This is why we selected the criterion of 6 m/s to differentiate the swell and wind-wave dominated cases in the ERS SAR image. Strictly speaking, the wind speed criterion does not differentiate wind waves from swell in the sense of water wave dynamics, but only in relation to the SAR imaging mechanism of surface waves. Consistency of criteria in the dynamic and SAR-imaging senses should be investigated in future using SARs with different resolutions.

When the wind speed  $> 6$  m/s, there is a possibility that the wind-wave and swell co-exist in a SAR image, although we could not find any such a case in the match-up sub-images. The SAR-detected wind waves were produced only by the surface winds blowing from offshore. Generally speaking, in the coastal seas, the winds off the land cannot have long fetches for generating wind waves that can be detected in a SAR image.

The SAR-imaged swells in the coastal seas come from offshore, which is adapted to removed the 180 directional ambiguity in our processing method. Therefore, both the near-shore swells and wind waves imaged by SAR have similar propagation directions toward the coast-

line. In this case, the swell and wind waves generated by strong winds over a long distance may be merged and treated as a wind-wave dominated case in our study.

Since SAR can only image one part of the wave spectra because of its limited spatial resolution, validation of SAR wave spectra requires separation of scales while the wave heights from the wave gauge observation used in the present study are generated by integrating all the spectral components of surface waves. This raised a question: does the missing part of SAR spectra beyond the Nyquist wave number really become a source of systematic error in present validation for the wind wave dominated cases?

In order to answer this question, we investigated the effect of wave number cutoff due to SAR's resolution on the significant wave height by calculating ratios of the missing part of wave spectra to the total wave energy using the JONSWAP formulation. Figure 9(a) shows the calculated JONSWAP spectra for wind speeds higher than 6 m/s, and Fig. 9(b) shows the ratio of wave energy beyond the cutoff wave number (indicated as a dashed line in Fig. 9(a)) to the total wave energy. The wind speeds for nine wind-wave dominated cases and the wave energy ratios of the missing part to the total are plotted in Fig. 9(b). The ratio decreases with increasing wind speed. Except for the two lower wind cases (8.9 m/s and 10.0 m/s), the ratio is smaller than 20%. However, though the cut-off effect may not be significant, the missing part of the wave spectra contributes to the bias between the SAR wave height (HSAR) and in-situ wave height ( $H_{in-situ}$ ) as  $H_{in-situ} > HSAR$ . Since we found only nine match-up of wind wave dominated cases, statistical evaluation of this effect is difficult and is left for future studies.

## 5. Conclusions

Using the SAR image mode data, we have developed a system to retrieve surface wave parameters in the coastal seas around Japan. The wind speed information is derived from the SAR image, which is also used to derive of the SAR spectrum. The coastal wave gauges of NOWPHAS have provided high quality, in-situ measurements of the wave parameters for the analysis and validation of SAR-derived surface wave parameters. The following conclusions may be drawn.

1) Through careful examinations of SAR and in situ conditions, we generated 66 match-ups using the SAR sub-images (3.2 km × 3.2 km) and the in situ wave parameters. The corresponding SAR surface wind with 1 km-resolution is combined with them.

2) The cut-off wavelength depends on the nonlinearity in the wind-wave imaging mechanism. Our analyses show that, in the wind-wave dominated condition, the cutoff wavelength is proportional to the root of significant wave height. Although it is based on a limited data set, this result is consistent with the results of previous studies.

3) Our validation of SAR wave height shows that for the whole data set the bias is 0.09 m and SDE 0.61 m. The correlation coefficient between them is 0.78. The biases and the SDE for the wind-wave dominated cases (9 match-ups) are 0.19 m and 0.94 m and for the swell-dominated cases (57) 0.07 m and 0.53 m, respectively.

4) The surface wave directions from the SAR images and NOWPHAS agree with the averaged absolute deviation of 18.4°. The agreement trend does not depend on the wave height.

This is the first time that the validation of surface wave parameter retrieval from SAR image mode data in coastal seas has been performed. Unlike MPI and SPRA, the present method can extract the wave information without additional inputs under the reasonable assumption that the waves appearing in the SAR images propagate towards the coast. This assumption is used to resolve the 180° directional ambiguity of wave direction. Considering the imaging mechanism difference, the wind waves and swell are processed separately according to a differentiating standard, which depends solely on wind speed. Better separation criteria (e.g., wave age) may improve the wave parameter retrieval, but this is left for future studies. Although the retrieval system cannot provide the surface wave field in the coastal seas with the same accuracy as that in the open ocean, it does enable us to improve the result of wave forecast in the coastal seas by combining the wave information from the data source of SAR. These promising results will give new opportunities for more systematic studies of surface wave from SAR images in coastal seas.

## Acknowledgements

The authors are grateful to Dr. Teruhisa Shimada for the wind retrieval model and valuable discussion. The ERS-SAR data were provided by Japan Aerospace Exploration Agency. We are thankful for the constructive suggestions given by two anonymous reviewers, which will be very helpful in our future investigation. This study is supported by National Natural Science Foundation of China (No. 40606007; No. 40830959), Exploratory Research Program for Young Scientists of Tohoku University (Leader: Dr. Teruhisa Shimada) and the national basic research program of China (973 program, No. 2005CB422307).

## References

- Alpers, W. (1983): Monte Carlo simulations for studying the relationship between ocean wave and synthetic aperture radar image spectra. *J. Geophys. Res.*, **88**(C3), 1745–1759.
- Alpers, W. R. and K. Hasselmann (1982): Spectral signal-to-clutter and thermal noise properties of ocean wave imaging synthetic aperture radars. *Int. J. Remote Sens.*, **3**, 423–446.
- Alpers, W. R., D. B. Ross and C. L. Rufenach (1981): On the detectability of ocean surface wave by Real and Synthetic Aperture Radar. *J. Geophys. Res.*, **86**(C7), 6481–6498.
- Alpers, W., U. Paul and G. Gross (1998): Katabatic wind fields in coastal areas studied by ERS-1 synthetic aperture radar imagery and numerical modeling. *J. Geophys. Res.*, **103**, 7875–7886.
- Bruning, C., R. Schmidt and W. Alpers (1994): Estimation of the ocean wave-radar modulation transfer function from synthetic aperture radar imagery. *J. Geophys. Res.*, **99**(C5), 9803–9816.
- Collard, F., F. Ardhuin and B. Chapron (2005): Extraction of coastal ocean wave fields from SAR images. *IEEE Journal of Oceanic Engineering*, **30**(3), 526–533.
- Donelan, M. A., J. Hamilton and W. H. Hui (1985): Directional spectra of wind generated waves. *Philos. Trans. R. Soc.*, **315**, 509–562.
- Elgar, S., T. H. C. Herbers and R. T. Guza (1994): Reflection of ocean surface gravity waves from a natural beach. *J. Phys. Oceanogr.*, **24**(7), 1503–1511.
- Engen, G. and H. Johnsen (1995): SAR-ocean wave inversion using image cross spectra. *IEEE Trans. Geosci. Remote Sensing*, **33**, 1047–1056.
- Feindt, F., J. Schroter and W. Alpers (1986): Measurement of the ocean wave-radar modulation transfer function at 35 GHz from a sea based platform in the North Sea. *J. Geophys. Res.*, **91**(C8), 9701–9708.
- Furevik, B. R., O. M., Johannessen and A. D. Sandvik (2002): SAR retrieved winds in polar regions—Comparison with in situ data and atmospheric model output. *IEEE Trans. Geosci. Remote Sensing*, **40**, 1720–1732.
- Hasselmann, D. E., M. Dunckel and J. A. Ewing (1980): Directional wave spectra observed during JONSWAP 1973. *J. Phys. Oceanogr.*, **10**, 1264–1280.
- Hasselmann, K. and S. Hasselmann (1991): On the nonlinear mapping of an ocean wave spectrum into a synthetic aperture radar image spectrum and its inversion. *J. Geophys.*

- Res.*, **96**(C6), 10713–10729.
- Hasselmann, K., T. P. Barnett, E. Bouws, H. Carlson, D. E. Cartwright, K. Enke, J. A. Ewing, H. Gienapp, D. E. Hasselmann, P. Kruseman, A. Meerburg, P. Müller, D. J. Olbers, K. Richter, W. Sell and H. Walden (1973): Measurements of wind-wave growth and swell decay during the Joint North Sea Wave Project (JONSWAP). *Erganzungsheft Deut Hydrogr Zeit*, **12**, 1–95.
- Hasselmann, K., R. K. Raney, W. J. Plant, W. Alpers, R. A. Shuchman, D. R. Lyzenga, C. L. Rufenach and M. J. Tucker (1985): Theory of synthetic aperture radar ocean imaging: a MARSEN view. *J. Geophys. Res.*, **90**(C3), 4659–4686.
- Hasselmann, S., C. Bruning, K. Hasselmann and P. Heimbach (1996): An improved algorithm for the retrieval of ocean wave spectra from synthetic aperture radar image spectra. *J. Geophys. Res.*, **101**(C7), 16615–16629.
- Johnsen, H., G. Engen, K. Hogda, B. Chapron and Y. Desnos (1999): Validation of ENVISAT wave mode level 1b and level 2 product using ERS SAR data. *Proceedings of the CEOS SAR Workshop, Toulouse, 26–29 October 1999, ESA SP-450*, 59–64.
- Kerbaol, V., B. Chapron and P. M. Vachon (1998): A global analysis of ERS-1/2 SAR wave mode images. *J. Geophys. Res.*, **103**, 7833–7846.
- Krogstad, H. E., O. Samset and P. M. Vachon (1994): Generalizations of the non-linear ocean-SAR transform and a simplified SAR inversion algorithm. *Atmosphere-Ocean*, **32**(1), 62–82.
- Lyzenga, D. R. (1986): Numerical simulation of synthetic aperture radar image spectra for ocean waves. *IEEE Trans. Geosci. Remote Sensing*, **GE-24**(6), 863–872.
- Mastenbroek, C. and C. F. de Valk (2000): A semiparametric algorithm to retrieve ocean wave spectra from synthetic aperture radar. *J. Geophys. Res.*, **105**, 3497–3516.
- Monaldo, F. M. and R. C. Beal (1998): Comparison of SIR-C SAR wavenumber spectra with WAM model predictions. *J. Geophys. Res.*, **103**(C9), 18815–18825.
- Nagai, T. and K. Nukada (2004): Recent improvement of real-time coastal wave-tide information system in Japan. *Workshop on Wave, Tide Observation and Modelings in the Asia-Pacific Region*, 1–12.
- Pan, F. and R. B. Smith (1999): Gap winds and wakes: SAR observations and numerical simulations. *J. Atmos. Sci.*, **56**, 905–923.
- Schulz-Stellenfleth, J. and S. Lehner (2002): Spaceborne synthetic aperture radar observation of ocean waves traveling into sea ice. *J. Geophys. Res.*, **107**(C8), 3106, 10.1029/2001JC00837.
- Schulz-Stellenfleth, J., S. Lehner and D. Hoja (2005): A parametric scheme for the retrieval of two-dimensional ocean wave spectra from synthetic aperture radar look cross spectra. *J. Geophys. Res.*, **110**, C05004, doi:10.1029/2004JC002822.
- Shimada, M. (1999): Verification processor for SAR calibration and interferometry. *Adv. Space Res.*, **23**(8), 1477–1486.
- Shimada, T. and H. Kawamura (2005): Statistical compartmentalization of surface wind field over coastal seas using high-resolution SAR-derived winds. *Geophys. Res. Lett.*, **32**, L05607, doi:10.1029/2004GL022231.
- Shimada, T., H. Kawamura and M. Shimada (2003): An L-band geophysical model function for SAR wind retrieval using JERS-1 SAR. *IEEE Trans. Geosci. Remote Sensing*, **41**(3), 518–531.
- Shimada, T., H. Kawamura, M. Shimada, I. Watabe and S. Iwasaki (2004): Evaluation of JERS-1 SAR Images from a coastal wind retrieval point of view. *IEEE Trans. Geosci. Remote Sensing*, **42**(3), 491–500.
- Vachon, P. W., H. E. Krogstad and J. S. Paterson (1994): Airborne and spaceborne Synthetic Aperture Radar observation of ocean waves. *Atmosphere-Ocean*, **32**(1), 83–112.
- Voorrips, A. C., C. Mastenbroek and B. Hansen (2001): Validation of two algorithms to retrieve ocean wave spectra from ERS synthetic aperture radar. *J. Geophys. Res.*, **106**(C8), 16825–16840.
- Wright, J. W. (1978): Detection of ocean waves by microwave radar: The modulation of short gravity-capillary waves. *Boundary-Layer Meteorology*, **13**, 87–105.
- Yamaguchi, S. and H. Kawamura (2005): Influence of orographically steered winds on Mutsu Bay surface currents. *J. Geophys. Res.*, **110**(9), Art. No. C09010.